arXiv:2101.06568v1 [cond-mat.soft] 17 Jan 2021

Learning hydrodynamic equations for active matter from particle simulations and experiments

Rohit Supekar, Boya Song, Alasdair Hastewell, Alexander Mietke,* and Jörn Dunkel†
Massachusetts Institute of Technology,
77 Massachusetts Avenue, Cambridge, MA 02139
(Dated: December 2, 2023)

Recent advances in high-resolution imaging techniques and particle-based simulation methods have enabled the precise microscopic characterization of collective dynamics in various biological and engineered active matter systems. In parallel, data-driven algorithms for learning interpretable continuum models have shown promising potential for the recovery of underlying partial differential equations (PDEs) from continuum simulation data. By contrast, learning macroscopic hydrodynamic equations for active matter directly from experiments or particle simulations remains a major challenge. Here, we present a framework that leverages spectral basis representations and sparse regression algorithms to discover PDE models from microscopic simulation and experimental data, while incorporating the relevant physical symmetries. We illustrate the practical potential through applications to a chiral active particle model mimicking swimming cells and to recent microroller experiments. In both cases, our scheme learns hydrodynamic equations that reproduce quantitatively the self-organized collective dynamics observed in the simulations and experiments. The inference framework makes it possible to measure hydrodynamic parameters directly and simultaneously from video data.

I. INTRODUCTION

Natural and engineered active matter, from cells [1], tissues [2] and organisms [3] to self-propelled particle suspensions [4, 5] and autonomous robots [6–8], exhibits complex dynamics across a wide range of length and time scales. Predicting the collective self-organization and emergent behaviors of such systems requires extensions of traditional theories that go beyond conventional physical descriptions of non-living matter [9–11]. Due to the inherent complexity of active matter interactions in multi-cellular communities [12, 13] and organisms [14], or even non-equilibrium chemical [15] or colloidal [4, 5, 16] systems, it becomes increasingly difficult and inefficient for humans to formulate and validate quantitative theories from first principles. A key question is therefore whether one can utilize computing machines [17] to identify interpretable systems of equations that elucidate the mechanisms underlying collective active matter dynamics.

Enabled by recent major advances in microscopic imaging [12, 14, 18, 19] and agent-based computational modeling [20], active matter systems can now be observed and analyzed at unprecedented spatiotemporal [21] resolution. To infer interpretable predictive theories, the high-dimensional data recorded in experiments or simulations have to be compressed and translated into low-dimensional models. Such learned models must faithfully capture the macroscale dynamics of the relevant collective properties. Macroscale properties can be efficiently encoded through hydrodynamic variables, continuous fields that are linked to the symmetries and conservation laws of the underlying microscopic system [10, 11]. Although much theoretical progress has been made in the field of dynamical systems learning over the last two decades [22–28], the inference of hydrodynamic models from particle data has remained largely unsuccessful in practice, not least due to severe complications arising from measurement noise, inherent fluctuations and self-organized scale-selection in active systems. Yet, extrapolating the current experimental revolution [4, 5, 12, 13, 18, 19], data-driven equation learning will become increasingly more important as simultaneous observations of physical, biological, and chemical properties of individual cells and other active units will become available in the near future [29, 30].

Learning algorithms for ordinary differential equations (ODEs) and partial differential equations (PDEs) have been proposed and demonstrated based on least-squares fitting [22, 23], symbolic regression [24, 25], and sparse regression [26, 27] combined with weak formulations [31], artificial neural networks [32, 33] and stability selection [28, 34]. These groundbreaking studies, however, focused primarily on synthetic data from *a priori* known continuum models, and recent coarse-graining applications have remained limited to ODEs [35] or one-dimensional PDEs [36, 37]. By contrast, it is still an open challenge to infer hydrodynamic PDE models directly from microscopic active matter simulations or experiments.

Here, we present a comprehensive learning framework that takes microscopic particle data as input and generates sparse interpretable predictive hydrodynamic models as output (Fig. 1). We demonstrate its practical potential in applications to active particle data from simulations and recent experiments [4]. In both cases we find that the learned hydrodynamic models predict the emergent collective dynamics not only qualitatively but also

* amietke@mit.edu
† dunkel@mit.edu

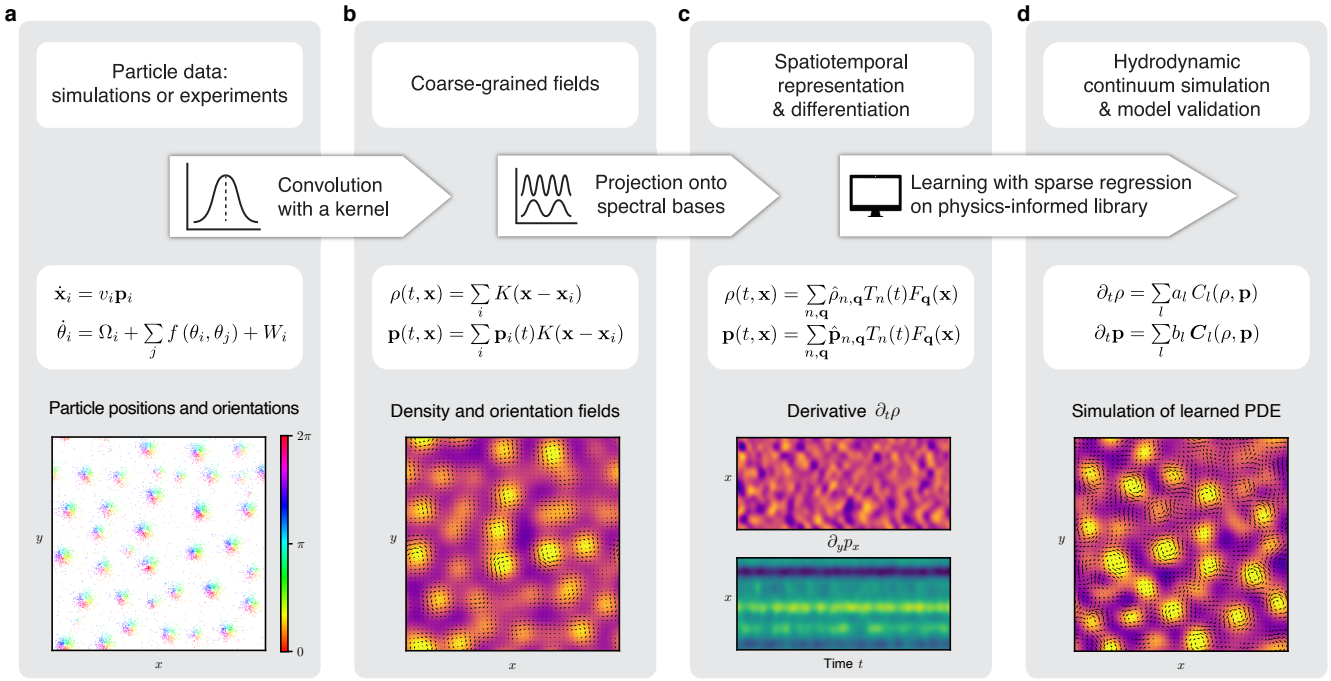

FIG. 1. Learning hydrodynamic models from particle simulations and experiments. **a**, Inputs are time-series data for particle positions $\mathbf{x}_i(t)$, particle orientations $\mathbf{p}_i(t) = (\cos\theta_i, \sin\theta_i)^\top$, etc., measured in simulations or experiments with microscale resolution (Sec. II A). **b**, Spatial kernel coarse-graining of the discrete microscopic variables provides continuous hydrodynamic fields, such as the density $\rho(t,\mathbf{x})$ or the polarization density $\mathbf{p}(t,\mathbf{x})$ (Sec. II B). **c**, Coarse-grained fields are sampled on a spatiotemporal grid and projected onto suitable spectral basis functions. Systematic spectral filtering (compression) ensures smoothly interpolated hydrodynamic fields, enabling efficient and accurate computation of spatiotemporal derivatives (Sec. II C). **d**, Using these derivatives, a library of candidate terms $C_l(\rho,\mathbf{p})$ and $\boldsymbol{C}_l(\rho,\mathbf{p})$ consistent with prior knowledge about conservation laws and broken symmetries is constructed. A sparse regression algorithm determines subsets of relevant phenomenological coefficients a_l and b_l (Sec. II D). The resulting hydrodynamic models are sparse and interpretable, and their predictions can be directly validated against analytic coarse-graining results (Sec. II E) or experiments (Sec. III). Bottom: Snapshots illustrating the workflow for microscopic data generated from simulations of chiral active Brownian particles [Eq. (1)].

quantitatively. Conceptually, this advance is made possible by leveraging spectral basis representations for systematic denoising and robust numerical differentiation. Our analysis further shows how insights from analytic coarse-graining calculations and prior knowledge of conservation laws and broken symmetries can enhance the robustness of automated equation discovery from microscopic data.

II. LEARNING FRAMEWORK

Our model learning approach combines recent advances in sparse PDE recovery [27, 34] with spectral filtering and compression [38–40]. We first demonstrate the key steps of the general framework (Fig. 1) for an experimentally motivated chiral active particle model, for which the hydrodynamic continuum equations were not known previously. Later on, we will apply the same methodology to infer a quantitative hydrodynamic model directly from video data recorded in recent microroller experiments [4] (Sec. III).

A. Active particle simulations

To generate challenging test data for the learning algorithm, we simulated a 2D system of interacting self-propelled chiral particles [41–45]. Microscopic models of this type are known to capture essential aspects of the experimentally observed self-organization of protein filaments [46, 47], bacterial swarms [21, 48, 49] and cell monolayers [50]. In the simulations, a particle i with orientation $\mathbf{p}_i = (\cos\theta_i, \sin\theta_i)^\top$ moved and changed orientation according to the Brownian dynamics

$$\dot{\mathbf{x}}_i = v_i \mathbf{p}_i, \tag{1a}$$

$$\dot{\theta}_i = \Omega_i + g \sum_{j \in \mathcal{N}_i} \sin(\theta_j - \theta_i) + \sqrt{2D_r}\eta_i, \tag{1b}$$

where $\eta_i(t)$ denotes orientational Gaussian white noise, with zero mean and $\langle \eta_i(t)\eta_j(t')\rangle = \delta_{ij}\delta(t-t')$, modulated by the rotational diffusion constant D_r. The parameter $g > 0$ determines the alignment interaction strength between particles i and j within a neighbourhood $\mathcal{N}_i$ of radius R. The self-propulsion speed $v_i \geq 0$ and orientational rotation frequency $\Omega_i \geq 0$ were drawn from

a joint distribution $p(v_i, \Omega_i)$ (App. A 1). This heuristic distribution was chosen such that long-lived vortex states, similar to those observed in swimming sperm cell suspensions [51], formed spontaneously from arbitrary random initial conditions (Fig. 2a). Emerging vortices are left-handed for $\Omega_i \geq 0$, and their typical size is $\sim \langle v_i \rangle_p / \langle \Omega_i \rangle_p$, where $\langle \cdot \rangle_p$ denotes an average over the parameter distribution $p(v_i, \Omega_i)$. We simulated Eq. (1) in non-dimensionalized form, choosing the interaction radius R as reference length and $R/\langle v_i \rangle_p$ as time scale. Accordingly, we set $R = 1$ and $\langle v_i \rangle_p = 1$ from now on. Simulations were performed for $N = 12,000$ particles on a periodic domain of size 100×100 (Fig. 2a).

From a learning perspective, this model poses many of the typical challenges that one encounters when attempting to infer hydrodynamic equations from active matter experiments: spontaneous symmetry breaking and mesoscale pattern formation, microscopic parameter variability, noisy dynamics, anisotropic interactions, and so on. Indeed, similar to many experimental systems, it is not even clear *a priori* whether or not Eqs. (1) permit a quantitative description in terms of a sparse hydrodynamic continuum model.

B. Hydrodynamic fields

Given particle-resolved data, hydrodynamic fields are obtained by coarse-graining. A popular coarse-graining approach is based on convolution kernels [52, 53], weight functions that translate discrete fine-grained particle densities into continuous fields, analogous to the point spread function of a microscope. For example, given the particle positions $\mathbf{x}_i(t)$ and orientations $\mathbf{p}_i(t)$, an associated particle number density field $\rho(t, \mathbf{x})$ and polarization density field $\mathbf{p}(t, \mathbf{x})$ can be defined by

$$\rho(t, \mathbf{x}) = \sum_i K\left[\mathbf{x} - \mathbf{x}_i(t)\right], \tag{2a}$$

$$\mathbf{p}(t, \mathbf{x}) = \sum_i K\left[\mathbf{x} - \mathbf{x}_i(t)\right] \mathbf{p}_i(t). \tag{2b}$$

The symmetric kernel $K(\mathbf{x})$ is centered at $\mathbf{x} = 0$ and normalized, $\int d^2\mathbf{x}\ K(\mathbf{x}) = 1$, so that the total number of particles is recovered from $\int d^2\mathbf{x}\, \rho(t, \mathbf{x}) = N$. Equations (2) generalize to higher tensorial density fields in a straightforward manner, and can be readily adapted to accommodate different boundary conditions (App. A 2).

We found that, in the context of hydrodynamic model learning, the coarse-graining (2) with a Gaussian kernel $K(\mathbf{x}) \propto \exp[-|\mathbf{x}|^2/(2\sigma^2)]$ presents a useful preprocessing step that simplifies the use of fast transforms at later stages. In practice, the coarse-graining scale σ has to be chosen larger than the particle's mean-free path, but small enough to resolve the relevant collective structures. For the microscopic test data from Eq. (1), $\sigma = 5$ provides a sufficient resolution of the emerging vortex patterns (Fig. 2a, bottom panel).

C. Spatiotemporal representation and differentiation

A central challenge in PDE learning is the computation of spatial and temporal derivatives of the coarse-grained fields. Our framework exploits that hydrodynamic models aim to capture the long-wavelength dynamics of the slow collective modes [10]. This fact makes it possible to project the coarse-grained fields on suitable basis functions that additionally enable sparse representations (high compression), fast transforms and efficient differentiation. Here, we work with representations of the form

$$\rho(t, \mathbf{x}) = \sum_{n,\mathbf{q}} \hat{\rho}_{n,\mathbf{q}} T_n(t) F_{\mathbf{q}}(\mathbf{x}), \tag{3a}$$

$$\mathbf{p}(t, \mathbf{x}) = \sum_{n,\mathbf{q}} \hat{\mathbf{p}}_{n,\mathbf{q}} T_n(t) F_{\mathbf{q}}(\mathbf{x}), \tag{3b}$$

where $T_n(t)$ denotes a degree-n Chebyshev polynomial of the first kind [54, 55], $F_{\mathbf{q}}(\mathbf{x}) = \exp(2\pi i \mathbf{q} \cdot \mathbf{x})$ is a Fourier mode with wave vector $\mathbf{q} = (q_x, q_y)^\top$, and $\hat{\rho}_{n,\mathbf{q}}$ and $\hat{\mathbf{p}}_{n,\mathbf{q}}$ are complex mode coefficients (Fig. 2b). Generally, the choice of the basis functions should be adapted to the spatiotemporal boundary conditions of the microscopic data (Sec. III).

The spectral representation (3) enables the efficient and accurate computation of space and time derivatives [56]. Preprocessing via spatial coarse-graining (Sec. II B) ensures that the mode coefficients $\hat{\rho}_{n,\mathbf{q}}$ and $\hat{\mathbf{p}}_{n,\mathbf{q}}$ decay fast for $|\mathbf{q}| \gg 1/(2\pi\sigma)$ (Fig. 2b, left). Furthermore, focusing on the slow hydrodynamic modes, we can filter out the fast modes with $n > n_0$ by keeping only the dominant Chebyshev terms in Eq. (3). The cut-off value n_0 can usually be directly inferred from a characteristic steep drop-off in the power spectrum of the data, which signals the transition to hydrodynamically irrelevant fast fluctuations [57] (Fig. 2b, right). Choosing n_0 according to this criterion yields accurate, spatiotemporally consistent derivatives as illustrated for the kymographs of the derivative fields $\partial_t \rho$ and $-\nabla \cdot \mathbf{p}$, which are essential to capture mass conservation. More generally, combining kernel-based and spectral coarse-graining also mitigates measurement noise, enabling a direct application to experimental data (Sec. III).

D. Inference of hydrodynamic equations

To infer hydrodynamic models that are consistent with the coarse-grained projected fields (3), we build on a recently proposed sparse regression framework [26, 27]. The specific aim is to determine sparse PDEs for the density and polarization dynamics of the form

$$\partial_t \rho = \sum_l a_l\, C_l(\rho, \mathbf{p}), \tag{4a}$$

$$\partial_t \mathbf{p} = \sum_l b_l\, \boldsymbol{C}_l(\rho, \mathbf{p}). \tag{4b}$$

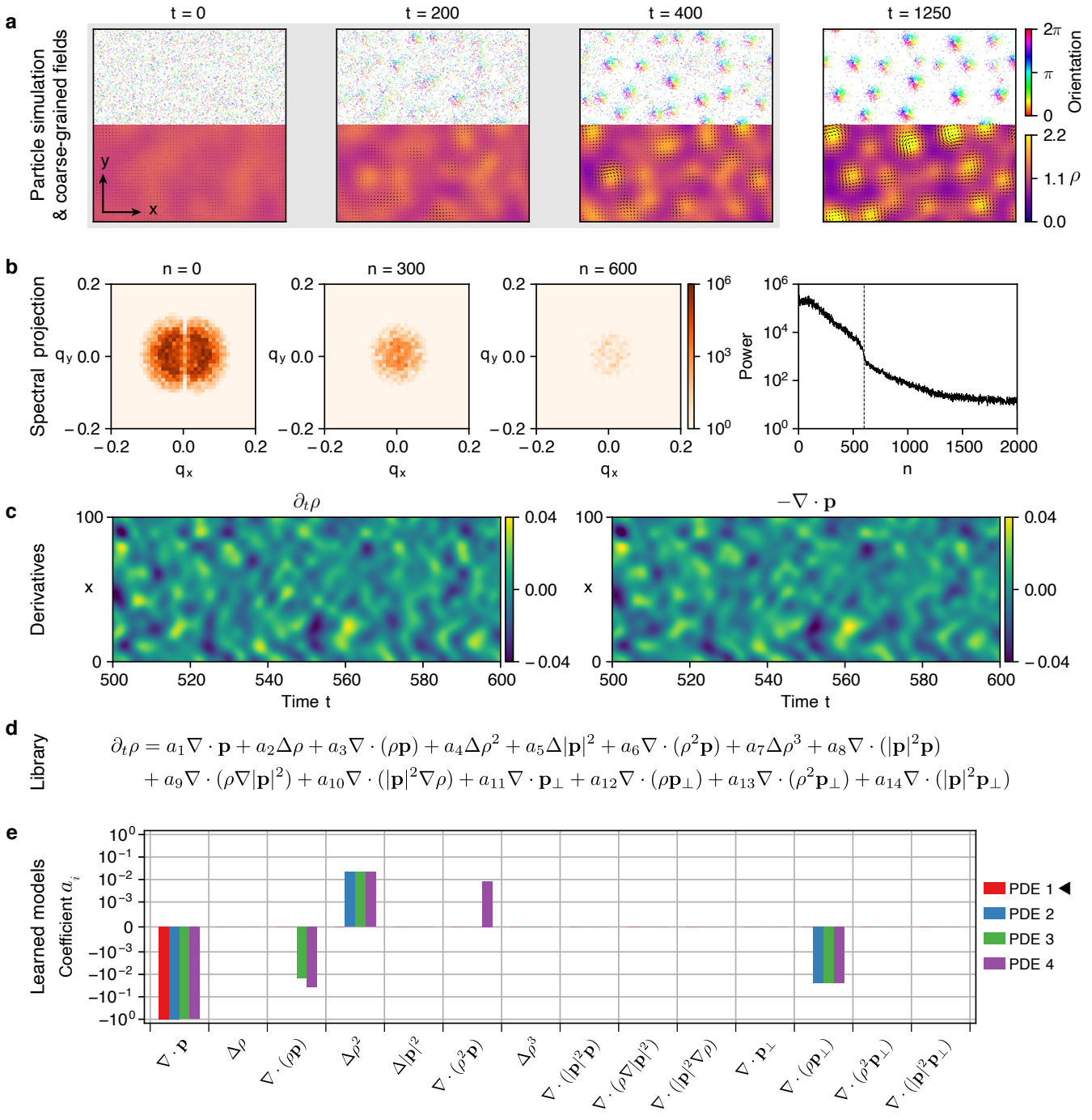

FIG. 2. Learning mass conservation dynamics. **a**, Top: Time evolution of positions and orientations of 12,000 particles following the dynamics in Eq. (1). Bottom: Coarse-grained density ρ (color code) and polarization field $\mathbf{p}$ (arrows). Starting from random initial conditions ($t = 0$), a long-lived vortex pattern with well-defined handedness emerges ($t = 1250$). Training data were randomly sampled from the time window $t \in [40, 400]$, enclosed within the gray box. Domain size: 100×100. **b**, Slices through the power spectrum $S_{x;n,\mathbf{q}} = |\mathbf{e}_x \cdot \hat{\mathbf{p}}_{n,\mathbf{q}}|^2$ for different values of the Chebyshev polynomial order $n \in \{0, 300, 600\}$, corresponding to modes with increasing temporal frequencies. The rightmost panel depicts the total spectral power $\sum_{\mathbf{q}} S_{x;n,\mathbf{q}}$ [see Eq. (3b)] of each Chebyshev mode n. The slowly decaying long tail of fast modes indicates a regime in which fluctuations dominate over a smooth signal. The cut-off $n_0 = 600$ removes these modes, in line with the goal to learn a hydrodynamic model for the slow long-wavelength modes. **c**, Kymographs of the spectral derivatives $\partial_t \rho$ and $-\nabla \cdot \mathbf{p}$ at $y = 50$, obtained from the spectrally truncated data. **d**, Mass conservation in the microscopic system restricts the physics-informed candidate library to terms that can be written as divergence of a vector field. **e**, Learned phenomenological coefficients a_l of PDEs with increasing complexity (decreasing sparsity) (App. C). PDE 1 (◀) is given by $\partial_t \rho = a_1 \nabla \cdot \mathbf{p}$ with $a_1 = -0.99$. As PDE 1 is the sparsest PDE that agrees well with analytic coarse-graining results (Tab. I), it is selected for the hydrodynamic model.

The candidate library terms $\{C_l(\rho, \mathbf{p})\}$ and $\{\boldsymbol{C}_l(\rho, \mathbf{p})\}$ are functions of the fields and their derivatives, which can be directly evaluated at various sample points using the spectral representation (3). Equations (4) thus define a linear system for the phenomenological coefficients a_l and b_l, and the objective is to find sparse solutions such that the resulting hydrodynamic model recapitulates the collective particle dynamics.

Learned hydrodynamic models must respect the symmetries of the underlying microscopic dynamics. Prior knowledge of such symmetries can greatly accelerate the inference process by placing constraints on the model parameters a_l and b_l. The learning ansatz (4b) already assumes global rotational invariance by using identical coefficients b_l for the x and y components of the polarization field equations. Generally, coordinate-independence of hydrodynamic models demands that the dynamical fields and the library functions C_l, $\boldsymbol{C}_l$, etc. have the correct scalar, vectorial or tensorial transformation properties. This fact imposes stringent constraints on permissible libraries, as do microscopic conservation laws.

1. *Symmetries and conservation laws: Generating a physics-informed candidate library*

Whenever prior knowledge about (broken) symmetries and conservation laws is available, it should inform the candidate library construction to ensure that the PDE learning is performed within a properly constrained model space. For example, the active particle model in Eq. (1) describes a chiral dynamical system with intrinsic microscopic rotation rates $\Omega_i \geq 0$. The space of valid hydrodynamic models therefore includes PDEs in which the mirror symmetry is explicitly broken. Formally, this implies the Levi-Civita symbol ϵ_{ij} can be used to generate pseudo-tensorial objects such as $\mathbf{p}_\perp := \boldsymbol{\epsilon}^\top \cdot \mathbf{p} = (-p_y, p_x)^\top$ and $\nabla_\perp := \boldsymbol{\epsilon}^\top \cdot \nabla = (-\partial_y, \partial_x)^\top$, that have to be included in the construction of the candidate libraries $\{C_l(\rho, \mathbf{p})\}$ and $\{\boldsymbol{C}_l(\rho, \mathbf{p})\}$.

Additional constraints on the scalar library terms $\{C_l(\rho, \mathbf{p})\}$ in Eq. (4a) arise from particle number conservation, which is known to hold for many experimental active matter systems as well as for microscopic models such as Eq. (1). In this case, it suffices to consider functions C_l that can be written as the divergence of a vector field that represents some flux contribution. In the application below, we included fluxes up to first order in derivatives and third order in the fields (Fig. 2d); if needed, this scalar library can be easily extended.

The vectorial library $\{\mathbf{C}_l(\rho, \mathbf{p})\}$ for the chiral polarization dynamics, Eq. (4b), cannot be constrained further by symmetries or conservation laws. Mechanical substrate interactions with the environment as invoked by the microscopic model (1) and present in many active matter experiments explicitly break Galilean invariance, leading to external forces and torques whose form is not known *a priori*. We therefore included in Eq. (4b) also vector fields that cannot be written as a divergence, such as $\mathbf{p}_\perp$, $\rho\mathbf{p}$ or $(\mathbf{p} \cdot \nabla)\mathbf{p}$, in our candidate library $\{\mathbf{C}_l(\rho, \mathbf{p})\}$.

In general, higher order terms and terms including derivatives can be systematically constructed from the basic set of available fields and operators $\mathcal{B} = \{\rho, \mathbf{p}, \mathbf{p}_\perp, \nabla, \nabla_\perp\}$. We illustrate the general procedure for an example library containing up to cubic terms from $\mathcal{B}$. The first step is to write the list of distinct rank-2 tensors

$$\mathcal{S} = \{s\mathbb{I}, s\boldsymbol{\epsilon}, \mathbf{pp}, \mathbf{pp}_\perp, \mathbf{p}_\perp\mathbf{p}_\perp, \nabla\mathbf{p}, \nabla\mathbf{p}_\perp, \nabla_\perp\mathbf{p}, \nabla_\perp\mathbf{p}_\perp\},$$

where $s \in \{1, \rho, \rho^2, \nabla \cdot \mathbf{p}, \nabla \cdot \mathbf{p}_\perp\}$ represents one of the linearly independent scalars that can be formed from elements in $\mathcal{B}$. From any tensor $\boldsymbol{\Sigma} \in \mathcal{S}$ and its transpose, we can then generate vectorial terms $\mathbf{C}_l$ by forming scalar products with the elements in $\mathcal{B}$. In particular, $\nabla \cdot \boldsymbol{\Sigma}$ and $\nabla_\perp \cdot \boldsymbol{\Sigma}$ yield possible contributions from internal stresses and torques due to alignment interactions, while $\boldsymbol{\Sigma} \cdot \mathbf{p}$ and $\boldsymbol{\Sigma} \cdot \mathbf{p}_\perp$ correspond to substrate-dependent interactions.

For pattern-forming systems with emergent length scale selection, the library should be extended to include Swift-Hohenberg-type [58] terms $\Delta^2\mathbf{p}$, $\Delta^2\mathbf{p}_\perp$, etc. [59, 60]. Such terms can stabilize small-wavelength modes and, combined with $\Delta\mathbf{p}$ and $\Delta\mathbf{p}_\perp$, can give rise to patterns of well-defined length [58]. A nematically restricted 19-term library used to learn the polarization dynamics for the chiral particle model from Eq. (1) is summarized in Fig. 3c.

2. *Sparse model learning*

To determine the hydrodynamic parameters a_l and b_l in Eqs. (4), we randomly sampled the coarse-grained fields $\rho(t, \mathbf{x})$ and $\mathbf{p}(t, \mathbf{x})$ and their derivatives at $\sim 10^6$ space-time points within a predetermined learning interval (App. A). Generally, the success or failure of hydrodynamic model learning depends crucially on the choice of an appropriate space-time sampling interval. As a guiding principle, learning should be performed during the relaxation stage, when both time and space derivatives show the most substantial variation.

Evaluating Eqs. (4a) and (4b) at all sample points yields linear systems of the form $\mathbf{U}_t = \boldsymbol{\Theta}\boldsymbol{\xi}$, where the vector $\mathbf{U}_t$ contains the time derivatives (App. A 3). The columns of the matrix $\boldsymbol{\Theta}$ hold the numerical values of the library terms $C_l(\rho, \mathbf{p})$ and $\boldsymbol{C}_l(\rho, \mathbf{p})$ computed from the spectral representations (3). The aim is to infer a parsimonious model so that the vector $\boldsymbol{\xi}$ containing the hydrodynamic parameters a_l or b_l is sparse. In this case, the corresponding PDE only contains a subset of the library terms, and we refer to the total number of terms in a PDE as its *complexity*.

To estimate sparse parameters $\boldsymbol{\xi}$, we used the previously proposed sequentially thresholded least-squares (STLSQ) algorithm from SINDy [26]. STLSQ first finds the least-squares estimate $\hat{\boldsymbol{\xi}} = \arg\min_{\boldsymbol{\xi}} ||\mathbf{U}_t - \boldsymbol{\Theta}\boldsymbol{\xi}||_2^2$.

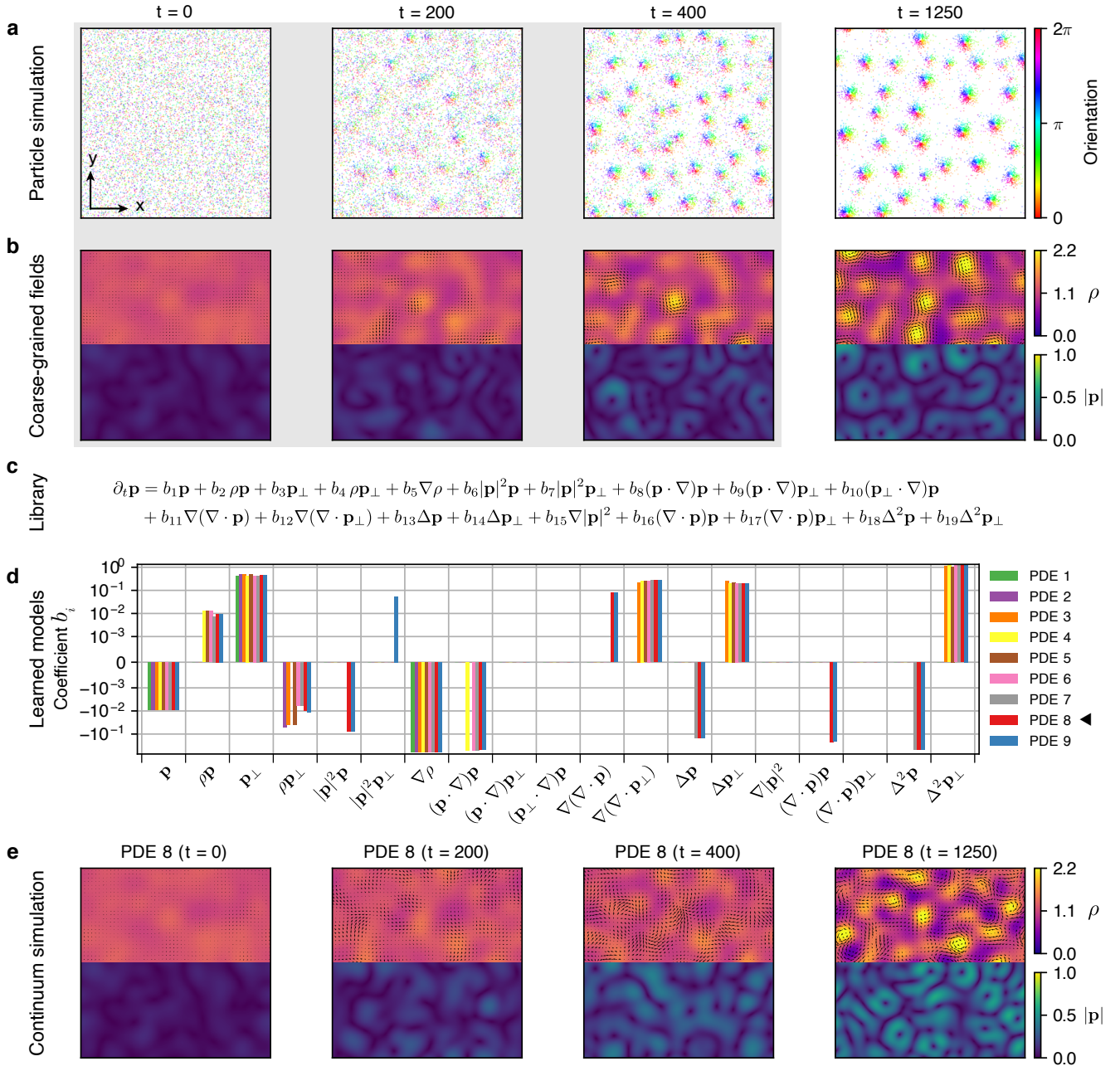

FIG. 3. Learning polarization dynamics. **a**, Same particle dynamics as in Fig. 2**a** for visual reference. **b**, Top: Coarse-grained density and polarization field as in Fig. 2**a**. Bottom: Magnitude $|\mathbf{p}|$ of the coarse-grained polarization field. Emerging vortices ($t = 400, 1250$) appear as ring-like patterns in $|\mathbf{p}|$. Training data were randomly sampled from the time window $t \in [40, 400]$, enclosed within the gray box. **c**, Physics-informed candidate library (with $b_1 = -D_r$) including terms constructed from $\mathbf{p}_\perp = (-p_y, p_x)^\top$, which are allowed due to the chirality of the microscopic system. **d**, Learned phenomenological coefficients b_l of PDEs with increasing complexity (App. C). For all PDEs, learned coefficients of the linear terms $\mathbf{p}_\perp$ and $\nabla\rho$ compare well with analytic predictions (Tab. I, App. B 2). **e**, Simulation of the final hydrodynamic model (PDE 8 for the polarization dynamics and PDE 1 in Fig. 2**e** for the density dynamics). Starting from random initial conditions ($t = 0$), long-lived vortex states emerge on a similar time scale, with similar spatial patterns, and with comparable density and polarization amplitudes as in the coarse-grained microscopic model data (**b**). Hydrodynamic models with PDEs sparser than PDE 8 do not form stable vortex patterns.

Subsequently, sparsity of $\hat{\boldsymbol{\xi}}$ is imposed by iteratively setting coefficients below a thresholding hyperparameter τ to zero. Adopting a stability selection approach [28, 34, 61, 62] in which τ is systematically varied over a regularization path $[\tau_{\max}, \tau_{\min}]$ (App. A 3), we obtain candidate PDEs of increasing complexity (Figs. 2e and 3d) whose predictions need to be validated against the phenomenology of the input data.

3. Performance improvements and pitfalls

Sparse regression-based learning becomes more efficient and robust if known symmetries or other available information can be used to reduce the number of undetermined parameters a_l and b_l in Eqs. (4). Equally helpful and important is prior knowledge of the relevant time and length scales. The coarse-grained field data need to be sampled across spatiotemporal scales that contain sufficient dynamical information; over-sampling in a steady-state typically prevents algorithms from learning terms relevant to the relaxation dynamics. Systems exhibiting slow diffusion time-scales can pose additional challenges. For example, generic analytic coarse-graining (App. B 1) shows that additive rotational noise as in Eq. (1b) implies the linear term $-D_r\mathbf{p}$ in the polarization dynamics Eq. (4b). If the diffusive time scale $1/D_r$ approaches or exceeds the duration of the sampling time interval, then the learned PDEs may not properly capture the relaxation dynamics of the polarization field. From a practical perspective, this is not a prohibitive obstacle, as the rotational diffusion coefficient D_r can be often measured independently from isolated single-particle trajectories [63]. In this case, fixing $-D_r\mathbf{p}$ in Eq. (4b) and performing the regression over the remaining parameters produced satisfactory learning results (see Fig. 3, where $1/D_r \sim 100$ is comparable to the length of the learning interval $t \in [40, 400]$).

E. Validation of learned models

The STLSQ algorithm with stability selection proposes PDEs of increasing complexity – the final learning step is to identify the sparsest acceptable hydrodynamic model among these (Fig. 1). This can be achieved by simulating all the candidate PDEs (App. A 4) and comparing their predictions against the original data and, if available, against analytic coarse-graining results (App. B).

For the microscopic particle model from Eq. (1), the sparsest learned PDE for the particle number density is $\partial_t\rho = a_1\nabla\cdot\mathbf{p}$ (Fig. 2e); this mass conservation equation is also predicted by analytic coarse-graining (App. B). The learned coefficient $a_1 = -0.99$ implies an effective number density flux $-a_1\mathbf{p} \approx \mathbf{p}$, which agrees very well with the analytic prediction $\langle v_i\rangle_p\mathbf{p} = \mathbf{p}$. Additional coefficients appearing in more complex models proposed by the algorithm are at least one order of magnitude smaller than a_1 (Fig. 2e). Hence, as part of a hydrodynamic description of the microscopic system Eq. (1), we adopt the minimal density dynamics $\partial_t\rho = a_1\nabla\cdot\mathbf{p}$ from now on.

TABLE I. Parameters of the hydrodynamic model learned for the microscopic dynamics in Eq. (1) and values predicted by analytic coarse-graining (App. B 2). $\langle\cdot\rangle_p$ denotes averages over the distribution $p(v_i, \Omega_i)$ of particle velocities v_i and rotation rates Ω_i (App. A 1).

Term	Learned value	Analytic coarse-graining
Density dynamics		
$a_1\nabla\cdot\mathbf{p}$	$a_1 = -0.99$	$-\langle v_i\rangle_p = -1.00$
Polarization dynamics		
$b_3\mathbf{p}_\perp$	$b_3 = 0.44$	$\langle v_i\Omega_i\rangle_p/\langle v_i\rangle_p = 0.50$
$b_5\nabla\rho$	$b_5 = -0.60$	$-\frac{1}{2}\langle v_i^2\rangle_p/\langle v_i\rangle_p = -0.57$

The sparsest learned PDE for the dynamics of the polarization field $\mathbf{p}$ only contains three terms. However, together with the density dynamics, the resulting hydrodynamic model is unstable and does not lead to the formation of vortex patterns. Our simulations showed that a certain level of complexity is required to reproduce the dynamics observed in the test data. In particular, there exists a unique sparsest model (PDE 8 in Fig. 3d) for which long-lived vortex states emerge from random initial conditions. The resulting hydrodynamic model exhibits density and polarization patterns quantitatively similar to those observed in the original particle system (Fig. 3a,b,e), which also form on a similar time scale. Furthermore, the learned coefficients of the linear terms $\sim \mathbf{p}_\perp$ and $\sim \nabla\rho$ agree well with the analytic predictions (Tab. I, App. B 2). As the learning only used coarse-grained field data in the time interval $t \in [40, 400]$, simulation results for $t > 400$ represent predictions of the learned hydrodynamic model (Fig. 3e). The close agreement between original data and the model simulations (Fig. 3b,e) show that the inference framework has succeeded in learning a previously unknown hydrodynamic description for a chiral polar active particle system with broadly distributed microscopic parameters.

III. LEARNING FROM EXPERIMENTAL DATA

The inference framework can be readily applied to experimental data. We illustrate this by learning a quantitative hydrodynamic model directly from a video recorded in a recent study [4] of driven colloidal suspensions (Fig. 4a). In these experiments, electrohydrodynamic instability enables micron-sized particles to self-propel with speeds up to a few millimeters per second across a surface. The rich collective dynamics of these so-called Quincke rollers [4, 64] provides a striking experimental realization of self-organization in active polar particle systems [10, 65, 66].

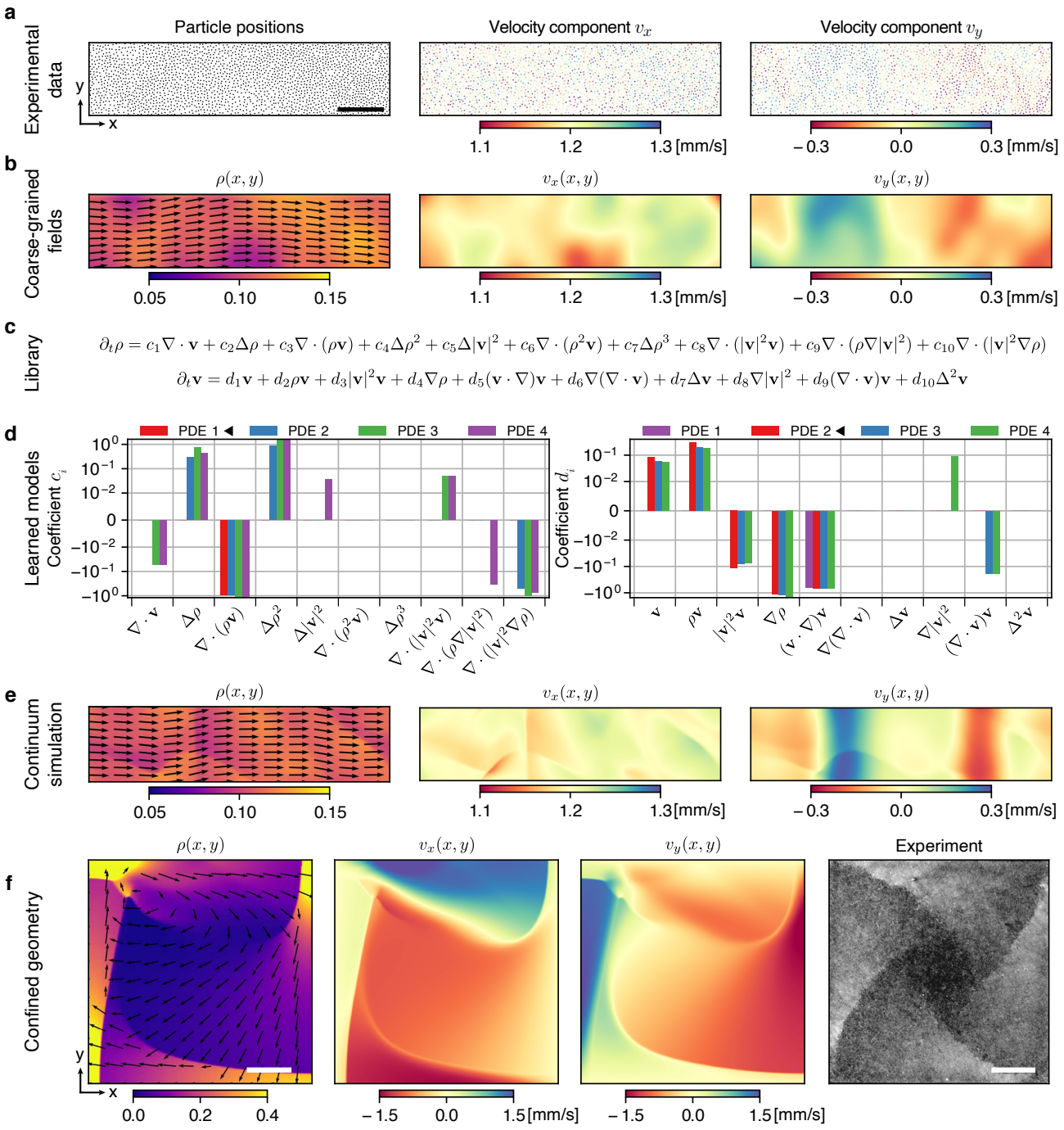

FIG. 4. Learning from active polar particle experiments. **a**, Snapshot of particle positions and velocity components of $\sim 2,200$ spontaneously moving Quincke rollers in a microfluidic channel [4]. Randomly sampled data points from ~ 580 such snapshots over a time duration of 1.4 s were used for the learning algorithm. Scale bar, 200 µm. **b**, Coarse-grained density field $\rho(t,\mathbf{x})$, expressed as the fraction of area occupied by the rollers with diameter $D_c = 4.8$ µm, and components $v_x(t,\mathbf{x})$ and $v_y(t,\mathbf{x})$ of the coarse-grained velocity field ($\sigma = 45$ µm). **c**, Physics-informed candidate libraries for the density and velocity dynamics, $\{\bar{C}_l(\rho,\mathbf{v})\}$ and $\{\bar{\boldsymbol{C}}_l(\rho,\mathbf{v})\}$, respectively [Eq. (5)]. These are the same libraries as shown in Figs. 2e and 3d, but without the chiral terms and replacing $\mathbf{p}\to\mathbf{v}$. **d**, Learned phenomenological coefficients c_l and d_l of the four sparsest PDEs for the density (left) and velocity (right) dynamics. The coefficients are non-dimensionalized with length scale σ and time scale σ/v_0, where $v_0 = 1.2\text{mm}\,\text{s}^{-1}$ is the average roller speed. PDE 1 for density dynamics corresponds to $\partial_t\rho = c_3\nabla\cdot(\rho\mathbf{v})$ with $c_3 \simeq -0.95$. PDE 2 for the velocity dynamics is shown in Eq. (6b). Learned coefficients compare well with the values reported in Ref. [4] (Tab. II). **e**, Simulation snapshot at $t = 1.8$ s of the learned hydrodynamic model (PDEs marked by ◀ in **d**) in a doubly periodic domain. Spontaneous flow emerges from random initial conditions, and exhibits density and velocity fluctuations that show similar spatial patterns and amplitudes as seen in the experiments (**a**). **f**, Simulation snapshots at $t = 18.5$ s of the same hydrodynamic model as in **e** on a square domain with reflective boundary conditions. The model predicts the emergence of a vortex-like flow permeated by density shock waves. This prediction agrees qualitatively with experimental observations (rightmost panel) of Quincke rollers in a 5mm × 5mm confinement with average density $\rho_0 \approx 0.1$ (Image credits: Alexandre Morin, Delphine Geyer, and Denis Bartolo). Scale bars, 200 µm (simulation) and 1 mm (experiment).

A. Coarse-graining and spectral representation of experimental data

To be able to apply the same model learning procedure, we first tracked the particle positions $\mathbf{x}_i(t)$ in Supplementary Video S2 of Ref. [4], which shows a weakly compressible suspension of Quincke rollers in a part of a racetrack-shaped channel (Fig. 4a). We then applied kernel coarse-graining [Eq. 2a, $\sigma = 45\mu$m] to the particle positions $\mathbf{x}_i(t)$ and velocities $\mathbf{v}_i(t) = \dot{\mathbf{x}}_i$ to obtain the density field ρ and the velocity field $\mathbf{v} = \mathbf{p}/\rho$. Accounting for the non-periodicity of the data, the fields ρ and $\mathbf{v}$ were projected on a Chebyshev polynomial basis [Eq. (3)] in time and space (Fig. 4b). Filtering out non-hydrodynamic fast modes with temporal mode numbers $n > n_0$, we found that the final learning results were robust for a large range of cut-off modes n_0 (App. C).

B. Physics-informed library

The goal is to learn a hydrodynamic model of the form

$$\partial_t \rho = \sum_l c_l \, \bar{C}_l(\rho, \mathbf{v}), \tag{5a}$$

$$\partial_t \mathbf{v} = \sum_l d_l \, \bar{\boldsymbol{C}}_l(\rho, \mathbf{v}), \tag{5b}$$

where $\bar{C}_l(\rho, \mathbf{v})$ and $\bar{\boldsymbol{C}}_l(\rho, \mathbf{v})$ denote library terms with coefficients c_l and d_l, respectively. The experimental Quincke roller system shares several key features with the particle model in Eq. (1), so the construction of the candidate libraries $\{\bar{C}_l(\rho, \boldsymbol{v})\}$ and $\{\bar{\boldsymbol{C}}_l(\rho, \mathbf{v})\}$ follows similar principles (Fig. 4c). Conservation of particle number implies that $\bar{C}_l$ can be written as divergences of vector fields. However, rollers do not explicitly break mirror symmetry, so chiral terms can be dropped from the $\{\bar{\boldsymbol{C}}_l(\rho, \mathbf{v})\}$ library, leaving the candidate terms in Fig. 4c.

C. Learned hydrodynamic equations and validation

The sparse regression algorithm proposed a hierarchy of hydrodynamic models with increasing complexity (Fig. 4d). The sparsest learned model that recapitulates the experimental observations is given by

$$\partial_t \rho = c_3 \nabla \cdot (\rho \mathbf{v}), \tag{6a}$$

$$\partial_t \mathbf{v} = d_1 \mathbf{v} + d_2 \rho \mathbf{v} + d_3 |\mathbf{v}|^2 \mathbf{v} + d_4 \nabla \rho + d_5 (\mathbf{v} \cdot \nabla) \mathbf{v}. \tag{6b}$$

Notably, Eqs. (6) contain all the relevant terms to describe the propagation of underdamped sound waves, a counter-intuitive, but characteristic feature of overdamped active polar particle systems [4].

Although the finite experimental observation window and imperfect particle tracking was expected to limit the accuracy of the learned models, the learned coefficient values agree well with corresponding parameters estimated in Ref. [4] by fitting a linearized Toner-Tu model to the experimental data (Tab. II). The coefficient $c_3 \simeq -0.95$ in the mass conservation equation is close to the theoretically expected value -1. The learned coefficient d_4 in the velocity Eq. (6b) is of similar magnitude but slightly less negative than the dispersion-based estimate in Ref. [4]. The learned coefficients d_1, d_2, and d_3, to our knowledge, had not been determined previously. Despite being inferred from a single video, these parameters yield a remarkably accurate prediction $v_0(\rho_0) = \sqrt{-(d_1 + d_2\rho_0)/d_3}$ for the typical roller speed as a function of the area fraction ρ_0 (Supplementary Fig. 4 in Ref [4] and Fig. 6). Similarly, the learned coefficient d_5 of the nonlinear advective term $\sim (\mathbf{v} \cdot \nabla)\mathbf{v}$, is in excellent agreement with the value reported in Ref [4]. Interestingly, $d_5 \neq -1$ reveals the broken Galilean invariance [9, 10] due to fluid-mediated roller-substrate interaction, a key physical aspect of the experimental system that is robustly discovered by the hydrodynamic model learning framework.

To validate the learned hydrodynamic model, we simulated Eqs. (6) on a periodic domain comparable to the experimental observation window (Fig. 4e, App. A 4). Starting from random initial conditions, spontaneously flowing states emerge, even though the spontaneous onset of particle flow is not a part of the experimental data from which the model was learned. The emergent density and flow patterns are quantitatively similar to the experimentally observed ones. In particular, the learned model predicts the formation of transverse velocity bands as seen in the experiments (Fig. 4b,e).

D. Predicting collective roller dynamics in confinement

Useful models can make predictions for a variety of experimental conditions. At minimum, if a learned hydrodynamic model captures the most relevant physics of an active system, then it should remain valid in different geometries and boundary conditions. To confirm this for the Quincke system, we simulated Eqs. (6) on a square domain using no-flux and shear-free boundary

TABLE II. Parameters of the learned hydrodynamic model for the Quincke roller system are close to values expected from analytic coarse-graining (*) and reported in Ref. [4] for experiments performed at mean area fraction $\rho_0 \approx 0.11$.

Term	Learned values	Ref. [4]
Density dynamics		
$c_3 \nabla \cdot (\rho \mathbf{v})$	$c_3 = -0.95$	-1.0*
Velocity dynamics		
$(d_1 + d_2\rho)\mathbf{v}$ $+d_3\lvert\mathbf{v}\rvert^2\mathbf{v}$	$\sqrt{\frac{d_1+d_2\rho_0}{-d_3}} = 1.21\,\mathrm{mm/s}$	$1.20\,\mathrm{mm/s}$
$d_4 \nabla \rho$	$d_4 = -1.62\,\mathrm{mm}^2/\mathrm{s}^2$	$-5.0 \pm 2.0\,\mathrm{mm}^2/\mathrm{s}^2$
$d_5 (\mathbf{v} \cdot \nabla)\mathbf{v}$	$d_5 = -0.67$	-0.7 ± 0.1

conditions (App. A 4). Starting from random initial conditions, our learned model predicts the formation of a vortex-like flow, permeated by four interwoven density shock waves, which arise from reflections at the boundary (Fig. 4f, left). Remarkably, this behavior has indeed been observed in experiments [64], in which Quincke rollers were confined within a square domain (Fig. 4f, right). These results demonstrate the practical potential of automated model learning for complex active matter systems.

IV. DISCUSSION & CONCLUSIONS

Leveraging spectral representations of field observables, we have presented a PDE learning framework that robustly identifies quantitative hydrodynamic models for the self-organized dynamics of active matter systems from both microscopic simulations and experimental data. This approach complements traditional analytic coarse-graining techniques [10, 42, 43, 49, 67] which require *ad hoc* moment closures to truncate infinite hierarchies of coupled mode equations (App. B). Analytic closures typically neglect correlations and rely on approximations that may not be valid in interacting active matter systems. Automated learning of hydrodynamic equations yields data-informed closure relations, while simultaneously providing quantitative measurements of phenomenological coefficients (viscosities, elastic moduli, etc.) from video data.

Successful model learning requires both good data and a good library. Good data need to sample all dynamically relevant length and time scales [68]. A good library is large enough to include all hydrodynamically relevant terms and small enough to enable robust sparse regression [28]. Since the number possible terms increases combinatorially with the number of fields and differential operators, library construction should be guided by prior knowledge of global, local, and explicitly broken symmetries. Such physics-informed libraries ensure properly constrained model search spaces, promising more robust and efficient sparse regression. Equally important is the use of suitable spectral field representations – without these an accurate evaluation of the library terms seems nearly impossible even for very-high quality data.

In view of the above successful applications, we expect that the computational framework presented here can be directly applied to a wide variety of passive and active matter systems. In parallel, there is vast potential for future enhancements by combining recent advances in sparse regression [34, 69] and weak formulations [31] with statistical information criteria [70] and cross-validation [71] for model selection. We therefore anticipate that many previously intractable physical and biological systems will soon find interpretable quantitative continuum descriptions that may reveal novel ordering and self-organization principles.

ACKNOWLEDGMENTS

We thank Keaton Burns for helpful advice on the continuum simulations, Henrik Ronellenfitsch for insightful discussions about learning methodologies, and the MIT SuperCloud [72] for providing us access to HPC resources. This work was supported by a MathWorks Engineering Fellowship (R.S.), a Graduate Student Appreciation Fellowship from the MIT Mathematics Department (B.S.), a Longterm Fellowship from the European Molecular Biology Organization (ALTF 528-2019, A.M.), a Postdoctoral Research Fellowship from the Deutsche Forschungsgemeinschaft (Project 431144836, A.M.), a Complex Systems Scholar Award from the James S. McDonnell Foundation (J.D.) and the Robert E. Collins Distinguished Scholarship Fund (J.D.).

Appendix A: Methods

1. Particle simulations

The microscopic model Eqs. (1) has been previously studied for fixed particle velocities $v_i = v_0$ and rotation frequencies $\Omega_i = \Omega_0$. In this scenario, particles form small clusters of aligned particles and each cluster orbits on a circle of radius $\sim v_0/\Omega_0$ [44]. To generate the microscopic test data used in Sec. II D, we considered instead a heuristic distribution $p(v_i, \Omega_i)$ for which particles spontaneously organize into proper vortices (Fig. 2a, top). It is convenient to define and draw from this distribution using propagation speeds v_i and the curvature radii $R_i = v_i/\Omega_i$ of a particle's noise-free trajectory as independent variables. In particular, we considered $\tilde{p}(v_i, R_i) \sim g(v_i; \mu_v, \sigma_v) g(R_i; \mu_R, \sigma_R)$, where $g(x; \mu_x, \sigma_x)$ represents a Gaussian normal distribution with mean μ_x and standard deviation σ_x. $\tilde{p}(v_i, R_i)$ then defines $p(v_i, \Omega_i)$ implicitly through the relation $v_i = \Omega_i R_i$. In units of the characteristic scales – mean velocity $\langle v_i \rangle_p$ and interaction radius R – the particle properties v_i and $\Omega_i = v_i/R_i$ used for simulating Eqs. (1) (Fig. 5) were drawn from $\tilde{p}(v_i, R_i)$ with $\mu_v = 1$ ($\langle v_i \rangle_{\tilde{p}} = \langle v_i \rangle_p = 1$), $\sigma_v = 0.4$, $\mu_R = 2.2$ and $\sigma_R = 1.7$. From these samples, we finally removed all particles with $\Omega_i > 1.4$.

For simulations of the microscopic model Eqs. (1), we set $g \simeq 0.35$ and $D_r \simeq 0.009$ ($\Rightarrow D_r \ll \langle \Omega_i \rangle_p$, $D_r \ll \langle v_i \rangle_p$) and initially placed particles randomly distributed and oriented on a domain of size 100×100 (in units of the interaction radius). Equations (1) were then numerically integrated using the Euler-Maruyama method with a time step of $dt \simeq 0.0176$. For the subsequent coarse-graining, the data were saved at time intervals of $\Delta t \simeq 0.44$.

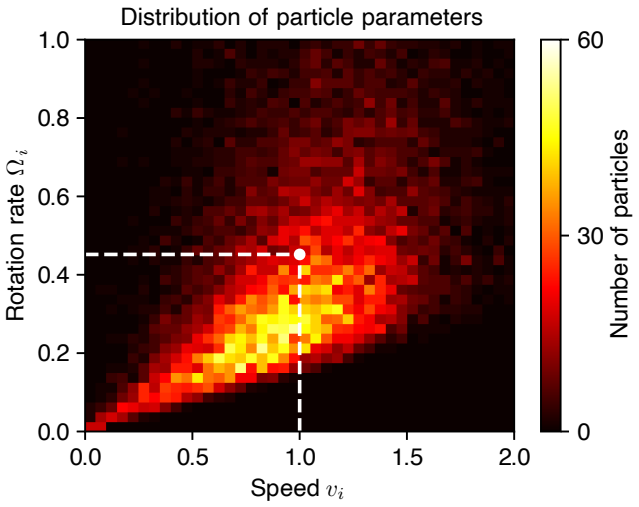

FIG. 5. Distribution of particle speeds v_i and rotation rates Ω_i used to simulate Eqs. (1). Those parameters were drawn from a heuristic distribution $p(v_i, \Omega_i)$ that is explained in more detail in Sec. A 1. The white marker and dashed lines depict the mean velocity $\langle v_i \rangle_p \simeq 1$ and $\langle \Omega_i \rangle_p \simeq 0.45$.

2. Kernel coarse-graining with periodic and non-periodic boundaries

For coarse-graining the discrete microscopic data through Eqs. (2), we used a 2D Gaussian kernel

$$K(\mathbf{x}) = (2\pi\sigma^2)^{-1} \exp\left(-|\mathbf{x}|^2/2\sigma^2\right). \tag{A1}$$

Periodicity of the coarse-grained fields for the test microscopic data (Sec. II B) was ensured by placing ghost particles periodically around the domain.

Coarse-graining in non-periodic domains (Sec. III) was performed by truncating and renormalizing the kernel. This was achieved by defining the integral over the non-periodic domain $\mathcal{X}$ to be $N(\mathbf{x}) = \int_{\mathcal{X}} d^2\mathbf{x}'\, K(\mathbf{x}' - \mathbf{x})$, and then replacing $K[\mathbf{x} - \mathbf{x}_i(t)]$ with $K[\mathbf{x} - \mathbf{x}_i(t)]/N(\mathbf{x})$ in Eqs. (2). This renormalization ensured that the coarse-grained density $\rho(t, \mathbf{x})$ integrated to the total particle number and strongly reduced artefacts near the boundary.

3. Sparse regression

To perform sparse regression using the sequentially thresholded least squares (STLSQ) algorithm [26], we used the same parameters when working with data from the test microscopic model (Sec. II A) as well as the Quincke roller experiments (Sec. III). The details of various steps in the learning framework are provided below.

Construction of linear systems: To construct the linear system $\mathbf{U}_t = \boldsymbol{\Theta}\boldsymbol{\xi}$, we randomly sampled the coarse-grained fields at $N_d = 5 \times 10^5$ time-space points. For clarity, the explicit forms of the linear systems that were constructed for Eqs. (4) are

$$\underbrace{\begin{bmatrix} \vdots \\ \partial_t \rho \\ \vdots \end{bmatrix}}_{\mathbf{U}_t (N_d \times 1)} = \underbrace{\begin{bmatrix} \vdots & & \vdots \\ \nabla\cdot\mathbf{p} & \cdots & \nabla\cdot(\rho\mathbf{p}_\perp) \\ \vdots & & \vdots \end{bmatrix}}_{\boldsymbol{\Theta}(N_d \times r)} \underbrace{\begin{bmatrix} a_1 \\ a_2 \\ \vdots \\ a_r \end{bmatrix}}_{\xi(r\times 1)}, \tag{A2a}$$

$$\underbrace{\begin{bmatrix} \partial_t p_x \\ \vdots \\ \hline \partial_t p_y \\ \vdots \end{bmatrix}}_{\mathbf{U}_t (2N_d \times 1)} = \underbrace{\left[\begin{array}{ccc} (\nabla\rho)_x & \cdots & ((\mathbf{p}\cdot\nabla)\mathbf{p})_x \\ \vdots & & \vdots \\ \hline (\nabla\rho)_y & \cdots & ((\mathbf{p}\cdot\nabla)\mathbf{p})_y \\ \vdots & & \vdots \end{array}\right]}_{\boldsymbol{\Theta}(2N_d \times m)} \underbrace{\begin{bmatrix} b_1 \\ b_2 \\ \vdots \\ b_s \end{bmatrix}}_{\boldsymbol{\xi}(m\times 1)}. \tag{A2b}$$

Here, the subscripts denote components of the vectors and r, m are the total number of library terms in each equation. The vertical dots denote the respective terms evaluated at different time-space $(t, \mathbf{x})$ locations. The linear system in Eq. (A2b) was generated by stacking data for the x- and y-components of the time-derivatives and the library terms. Such a construction enforced the same coefficients for both the components of the polarization equation, ensuring rotational invariance (coordinate-independence) of the learned PDE.

Pre-processing: Since the thresholding hyperparameter τ in STLSQ is agnostic to the scales of the library terms, as a pre-processing step, we performed transformations so that columns of the data matrix $\boldsymbol{\Theta}$ had zero mean and unit variance, and the time-derivative vector $\mathbf{U}_t$ had zero mean. The inferred coefficients were then multiplied by the standard deviation of the original columns to revert them back to the original scale.

Stability selection: With equal spacing on a $\log_{10}$ scale, we chose 40 values for τ over the regularization path $[\tau_{\max}, \epsilon\tau_{\max}]$. The value of $\tau_{\max}$ was chosen so that all the terms get thresholded out and ϵ was set to 10^{-2}. For every τ, the data were split into 200 sub-samples each with 50% randomly selected data points. Every library term was assigned an importance score as the fraction of sub-samples in which it was learned by STLSQ; in general, this importance score was larger for smaller values of τ. Along the regularization path, unique combinations of terms that had an importance score larger than 0.6 were considered and their coefficients were refitted to the full data. This procedure resulted in a small number of PDEs of increasing complexity (Figs. 2e, 3d, and 4d).

4. Continuum simulations

Continuum simulations were performed using the spectral PDE solver Dedalus [40] with four-step Runge-Kutta timestepping scheme RK443. Simulation of the PDEs learned from the microscopic test data (Fig. 3e) were done using 256×256 Fourier modes in a doubly periodic domain with time step 4×10^{-3}. The simulations

were initialized with the same initial conditions as in the coarse-grained particle data.

For the doubly periodic simulation of Eqs. (6) (Fig. 4e), we used 1024×1024 Fourier modes and time step 10^{-4}s. The initial conditions were random with mean density 0.11, and mean horizontal and vertical velocities, $0.1\,\mathrm{mm\,s^{-1}}$ and $0\,\mathrm{mm\,s^{-1}}$, respectively.

The simulation presented in Fig. 4f was performed on a confined square domain using the Sine/Cosine basis functions with 1024×1024 modes and time step 10^{-4}s. The basis combinations in the (x, y) directions were chosen to be (cos, cos) for density ρ, (sin, cos) for v_x and (cos, sin) for v_y. These imply that normal velocities, normal density gradients, and the transverse strain rate vanish at the domain boundaries. The simulations were initialized with random perturbations around a mean density of 0.11.

Since the learned model in Eqs. (6) generates density shock waves, we added numerical diffusivities of $10^{-4}\mathrm{mm}^2/\mathrm{s}$ (Fig. 4e) and $10^{-3}\mathrm{mm}^2/\mathrm{s}$ (Fig. 4f) in both density and velocity equation to avoid Gibb's ringing.

Appendix B: Analytic coarse-graining of the particle model

We describe two approaches to analytically determine mean-field approximations of the microscopic model Eqs. (1). These approaches (*i*) provide guidance for developing a physics-informed learning library, (*ii*) allow discussing our PDE learning framework as a tool to effectively infer moment closure relations, and (*iii*) predict the dependency of certain PDE coefficients on distributions of microscopic parameters, which can be used to validate learned hydrodynamic models.

1. Dynamic equation of the one-particle probability density

A commonly used approach to determine mean-field description of models such as Eqs. (1) is to find an approximate dynamic equation for the one-particle probability density [10, 42–44, 67, 73]

$$f(\theta, \mathbf{x}, t) = \sum_{i=1}^{N} \langle \delta\left(\theta - \theta_i(t)\right) \delta\left(\mathbf{x} - \mathbf{x}_i\right) \rangle, \tag{B1}$$

where $\langle \cdot \rangle$ denotes a Gaussian white noise average. Neglecting multiplicative noise and factorizing pair-correlations gives rise to a nonlinear integro-differential equation [42, 44] that can be transformed into an infinite hierarchy of coupled PDEs for the angular moments $f_n(\mathbf{x}, t)$ defined by

$$f_n(\mathbf{x}, t) = \int_0^{2\pi} d\theta f(\theta, \mathbf{x}, t) e^{in\theta}. \tag{B2}$$

For the microscopic model Eqs. (1) and equal swimming parameters $v_i = v_0$ and $\Omega_i = \Omega_0$ for all particle, this procedure leads to [42, 44]

$$\begin{aligned} &\partial_t f_n + \frac{v_0}{2}\left[\partial_x\left(f_{n+1} + f_{n-1}\right) - i\partial_y\left(f_{n+1} - f_{n-1}\right)\right] \\ &= n(i\Omega_0 - D_r n) f_n + \frac{gn\pi}{2}\left(f_{n-1} f_1 - f_{n+1} f_{-1}\right). \end{aligned} \tag{B3}$$

Each complex angular moment f_n can be identified as a mean-field variable that represents different orientational order parameters encoded by the probability density $f(\theta, \mathbf{x}, t)$ [10]. In particular, f_0 represents the particle number density ρ and $f_1 =: p_x + ip_y$ represents the polarization density $\mathbf{p} = (p_x, p_y)^\top$. These fields correspond to the coarse-graining information Eqs. (2) that our learning framework extracts explicitly from given microscopic data. For $n = 0$ and $n = 1$, we can therefore write Eqs. (B3) as

$$\partial_t \rho + v_0 \nabla \cdot \mathbf{p} = 0, \tag{B4a}$$

$$\partial_t \mathbf{p} + \frac{v_0}{2}(\nabla\rho + \nabla \cdot \mathbf{Q}) = \Omega_0 \mathbf{p}_\perp - D_r \mathbf{p} + \frac{g\pi}{2}\left(\rho\mathbb{I} - \mathbf{Q}\right) \cdot \mathbf{p}, \tag{B4b}$$

which also shows the coupling to the next higher mode $f_2 =: Q_{xx} + iQ_{xy}$, corresponding to the independent degrees of freedom of a nematic tensor. The chiral term $\sim \Omega_0 \mathbf{p}_\perp$ with $\mathbf{p}_\perp = (-p_y, p_x)^\top$ breaks the mirror symmetry. Terms constructed from $\mathbf{p}_\perp$ are therefore generally allowed in chiral systems and consequently included into the library Eqs. (4). Similarly, terms constructed from $\nabla_\perp = (-\partial_y, \partial_x)^\top$ can in general exist in chiral systems. However, many such terms can be expressed in terms of ∇, $\mathbf{p}$ and $\mathbf{p}_\perp$, for example $\nabla \cdot \mathbf{p} = \nabla_\perp \cdot \mathbf{p}_\perp$ and $\nabla \cdot \mathbf{p}_\perp = -\nabla_\perp \cdot \mathbf{p}$, both of which are included in the library Eq. (4a).

The final step that is key to analytically close the infinite hierarchy of Eqs. (B3) requires the introduction of moment closure assumptions [4, 42, 67]. Depending on the structure of the mode coupling, the resulting closure relation allows to express the nearest coupled modes with $|n| = k$ in terms of modes $|n| < k$ and neglects the remaining modes. For example, in the case of Eq. (B4) a moment closure assumption must provide an expression $\mathbf{Q}(\rho, \mathbf{p})$ [4, 42]. Our framework does not require explicit closure assumptions but instead takes a different route by inferring – directly from the data – an effective closure relation that best explains the observed systems dynamics.

2. Dynamic equations from conventional kernel coarse-graining

While the previous approach provides a clear coarse-graining strategy to find a closed set of PDEs from a system of stochastic ODEs with homogeneous microscopic parameters, it is more challenging to understand how

the phenomenological coefficients will depend on the distribution $p(v_i, \Omega_i)$ of microscopic kinetic parameters described in Sec. A 1. We therefore consider an alternative strategy, for which we write Eqs. (1) as

$$\frac{d\mathbf{x}_i}{dt} = v_i \mathbf{p}_i, \tag{B5a}$$

$$\frac{d\mathbf{p}_i}{dt} = \Omega_i \boldsymbol{\epsilon} \cdot \mathbf{p}_i + \mathbf{F}_i, \tag{B5b}$$

where $\boldsymbol{\epsilon} \cdot \mathbf{p}_i = \mathbf{p}_{i,\perp} = (-\sin\theta_i, \cos\theta_i)^\top$, and $\mathbf{F}_i$ contains forces from interactions and rotational diffusion. Taking directly the time derivative of the coarse-graining prescription Eq. (2a) and using Eq. (B5a), we find

$$\partial_t \rho(t, \mathbf{x}) + \nabla \cdot \mathbf{J}(t, \mathbf{x}) = 0, \tag{B6}$$

where we have defined a flux

$$\mathbf{J}(t, \mathbf{x}) = \sum_i K\left[\mathbf{x} - \mathbf{x}_i(t)\right] \, v_i \mathbf{p}_i. \tag{B7}$$

Using this definition and Eq. (B5b), we find a dynamic equation for $\mathbf{J}$ of the form

$$\partial_t \mathbf{J}(t, \mathbf{x}) + \nabla \cdot \boldsymbol{\sigma}(t, \mathbf{x}) = \mathbf{T}(t, \mathbf{x}) + \boldsymbol{\Phi}(t, \mathbf{x}). \tag{B8}$$

Here, we have defined the tensor and vector fields

$$\boldsymbol{\sigma}(t, \mathbf{x}) = \sum_i K\left[\mathbf{x} - \mathbf{x}_i(t)\right] \, v_i^2 \mathbf{p}_i(t)\mathbf{p}_i(t), \tag{B9a}$$

$$\mathbf{T}(t, \mathbf{x}) = \boldsymbol{\epsilon} \cdot \sum_i K\left[\mathbf{x} - \mathbf{x}_i(t)\right] \, v_i \Omega_i \mathbf{p}_i(t), \tag{B9b}$$

$$\boldsymbol{\Phi}(t, \mathbf{x}) = \sum_i K\left[\mathbf{x} - \mathbf{x}_i(t)\right] \, v_i \mathbf{F}_i(t). \tag{B9c}$$

Averaging the fields in Eq. (B7) and Eqs. (B9) over the particle parameter distribution $P(v_i, \Omega_i)$ yields

$$\langle \mathbf{J}(t, \mathbf{x}) \rangle_p = \left\langle \sum_i K\left[\mathbf{x} - \mathbf{x}_i(t)\right] v_i \mathbf{p}_i \right\rangle_p, \tag{B10a}$$

$$\langle \boldsymbol{\sigma}(t, \mathbf{x}) \rangle_p = \left\langle \sum_i K\left[\mathbf{x} - \mathbf{x}_i(t)\right] \, v_i^2 \, \mathbf{p}_i(t)\mathbf{p}_i(t) \right\rangle_p, \tag{B10b}$$

$$\langle \mathbf{T}(t, \mathbf{x}) \rangle_p = \left\langle \boldsymbol{\epsilon} \cdot \sum_i K\left[\mathbf{x} - \mathbf{x}_i(t)\right] v_i \Omega_i \, \mathbf{p}_i(t) \right\rangle_p, \tag{B10c}$$

$$\langle \boldsymbol{\Phi}(t, \mathbf{x}) \rangle_p = \left\langle \sum_i K\left[\mathbf{x} - \mathbf{x}_i(t)\right] \, v_i \mathbf{F}_i(t) \right\rangle_p. \tag{B10d}$$

We then adopt a moment factorization approximation

$$\langle \mathbf{J}(t, \mathbf{x}) \rangle_p \simeq \langle v_i \rangle_p \mathbf{p}, \tag{B11a}$$

$$\langle \boldsymbol{\sigma}(t, \mathbf{x}) \rangle_p \simeq \frac{1}{2} \langle v_i^2 \rangle_p \left(\rho \mathbb{I} + \mathbf{Q}\right), \tag{B11b}$$

$$\langle \mathbf{T}(t, \mathbf{x}) \rangle_p \simeq \langle v_i \Omega_i \rangle_p \mathbf{p}_\perp, \tag{B11c}$$

where we used the definition of the particle number density Eq. (2a), the polarization density Eq. (2b), and $|\mathbf{p}_i|^2 = 1$. Additionally, have defined in Eq. (B11b) a nematic moment of the form

$$\mathbf{Q} = \sum_i K\left[\mathbf{x} - \mathbf{x}_i(t)\right] \left[2\mathbf{p}_i(t)\mathbf{p}_i(t) - \mathbb{I}\right]. \tag{B12}$$

Finally, averaging Eqs. (B6) and (B8) over the microscopic parameter distributions and using Eqs. (B11), we obtain

$$\partial_t \rho + \langle v_i \rangle_p \nabla \cdot \mathbf{p} = 0, \tag{B13a}$$

$$\partial_t \mathbf{p} + \frac{\langle v_i^2 \rangle_p}{2\langle v_i \rangle_p} \left(\nabla \rho + \nabla \cdot \mathbf{Q}\right) = \frac{\langle v_i \Omega_i \rangle_p}{\langle v_i \rangle_p} \mathbf{p}_\perp + \langle v_i \rangle_p^{-1} \langle \boldsymbol{\Phi} \rangle_p. \tag{B13b}$$

From this, we can read of predictions about the coefficients we expect to find by the learning framework for the terms $\nabla \cdot \mathbf{p}$, $\nabla \rho$ and $\mathbf{p}_\perp$ (Tab. I).

Appendix C: Parameters of learned models

The parameters of the PDEs learned from simulations of the active polar particle model in Eq. (1) are summarized in Tab. III (density dynamics) and Tab. IV (polarization dynamics). For the experimental Quincke roller system [4], the learned hydrodynamic model parameters are given in Tab. V (density dynamics) and Tab. VI (velocity dynamics). Prediction of the ordered-state velocity as a function of the density obtained from the learned model in Eq. (6) is shown in Fig. 6.

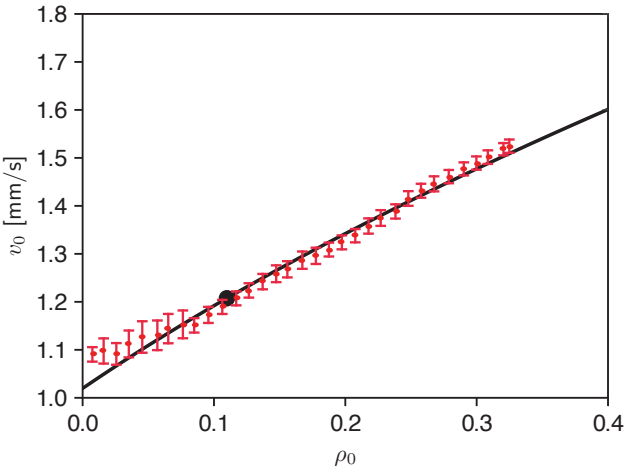

FIG. 6. Prediction for the velocity magnitude of the ordered state from the model in Eq. (6) learned from experimental data of self-propelled Quincke rollers (Supplementary Video 2 of Ref. [4]) with average area fraction $\rho_0 = 0.11$ (black dot). The solid line is the model prediction $v_0(\rho_0) = \sqrt{-(d_1 + d_2\rho_0)/d_3}$ for the typical roller speed with learned parameters d_1, d_2, d_3, and the red markers show the experimentally measured speed values from Supplementary Fig. 4 of Ref. [4].

TABLE III. Parameters a_l of the density dynamics PDE (Fig. 2d) learned from simulations the microscopic active particle system in Eq. (1). The sparsest model (◀) agrees well with the analytic coarse-graining prediction (Tab. I).

Term	PDE 1◀	PDE 2	PDE 3	PDE 4
$a_1\nabla\cdot\mathbf{p}$	-0.991	-0.991	-0.972	-0.957
$a_2\Delta\rho$	–	–	–	–
$a_3\nabla\cdot(\rho\mathbf{p})$	–	–	-0.015	-0.037
$a_4\Delta\rho^2$	–	0.022	0.022	0.022
$a_5\Delta\lvert\mathbf{p}\rvert^2$	–	–	–	–
$a_6\nabla\cdot(\rho^2\mathbf{p})$	–	–	–	0.008
$a_7\Delta\rho^3$	–	–	–	–
$a_8\nabla\cdot(\lvert\mathbf{p}\rvert^2\mathbf{p})$	–	–	–	–
$a_9\nabla\cdot(\rho\nabla\lvert\mathbf{p}\rvert^2)$	–	–	–	–
$a_{10}\nabla\cdot(\lvert\mathbf{p}\rvert^2\nabla\rho)$	–	–	–	–
$a_{11}\nabla\cdot\mathbf{p}_\perp$	–	–	–	–
$a_{12}\nabla\cdot(\rho\mathbf{p}_\perp)$	–	-0.026	-0.026	-0.026
$a_{13}\nabla\cdot(\rho^2\mathbf{p}_\perp)$	–	–	–	–
$a_{14}\nabla\cdot(\lvert\mathbf{p}\rvert^2\mathbf{p}_\perp)$	–	–	–	–

TABLE IV. Parameters b_l of the nine sparsest PDEs for the polarization dynamics (Fig. 3c), learned from simulations of the microscopic system in Eq. (1). PDE 8 (◀) reproduces the characteristic vortex dynamics as in the microscopic simulations (Fig. 3a,b,e) and the coefficients of the linear terms compare well with analytic coarse-graining predictions (Tab. I).

Term	PDE 1	PDE 2	PDE 3	PDE 4	PDE 5	PDE 6	PDE 7	PDE 8◀	PDE 9
$b_1\mathbf{p}$	-0.009	-0.009	-0.009	-0.009	-0.009	-0.009	-0.009	-0.009	-0.009
$b_2\rho\mathbf{p}$	–	–	–	0.013	0.013	0.013	0.007	0.009	0.009
$b_3\mathbf{p}_\perp$	0.414	0.476	0.477	0.428	0.478	0.436	0.436	0.440	0.441
$b_4\rho\mathbf{p}_\perp$	–	-0.050	-0.040	–	-0.040	-0.006	-0.006	-0.010	-0.012
$b_5\lvert\mathbf{p}\rvert^2\mathbf{p}$	–	–	–	–	–	–	–	-0.080	-0.080
$b_6\lvert\mathbf{p}\rvert^2\mathbf{p}_\perp$	–	–	–	–	–	–	–	–	0.054
$b_7\nabla\rho$	-0.638	-0.637	-0.600	-0.595	-0.601	-0.596	-0.596	-0.595	-0.595
$b_8(\mathbf{p}\cdot\nabla)\mathbf{p}$	–	–	–	-0.536	–	-0.510	-0.510	-0.463	-0.479
$b_9(\mathbf{p}\cdot\nabla)\mathbf{p}_\perp$	–	–	–	–	–	–	–	–	–
$b_{10}(\mathbf{p}_\perp\cdot\nabla)\mathbf{p}$	–	–	–	–	–	–	–	–	–
$b_{11}\nabla(\nabla\cdot\mathbf{p})$	–	–	–	–	–	–	–	0.078	0.077
$b_{12}\nabla(\nabla\cdot\mathbf{p}_\perp)$	–	–	0.225	0.265	0.248	0.265	0.270	0.277	0.277
$b_{13}\Delta\mathbf{p}$	–	–	–	–	–	–	-0.151	-0.155	-0.156
$b_{14}\Delta\mathbf{p}_\perp$	–	–	0.252	0.202	0.222	0.203	0.198	0.196	0.197
$b_{15}\nabla\lvert\mathbf{p}\rvert^2$	–	–	–	–	–	–	–	–	–
$b_{16}(\nabla\cdot\mathbf{p})\mathbf{p}$	–	–	–	–	–	–	–	-0.225	-0.213
$b_{17}(\nabla\cdot\mathbf{p})\mathbf{p}_\perp$	–	–	–	–	–	–	–	–	–
$b_{18}\Delta^2\mathbf{p}$	–	–	–	–	–	–	-0.475	-0.483	-0.484
$b_{19}\Delta^2\mathbf{p}_\perp$	–	–	1.100	1.197	1.085	1.212	1.215	1.235	1.243

TABLE V. Parameters c_l of the PDE for the density dynamics (Fig. 4c) learned from experimental data for self-propelled Quincke rollers (Supplementary Video 2 of Ref. [4]). The dimensions of the coefficients are such that $[\mathbf{v}]$ =mm/s and $[\rho] = 1$, where the density ρ represents the area fraction of rollers of diameter $D_c = 4.8\,\mu$m. The four sparsest PDEs are shown corresponding to the cut-off $n_0 \in \{50, 100\}$ above which the temporal Chebyshev modes in Eq. (3) are set to zero to ignore high frequencies. The sparsest PDEs (◀) have coefficients close to each other and agree well with the mass conservation equation obtained from analytic coarse-graining (Ref. [4]).

		$n_0 = 50$				$n_0 = 100$			
Term	Unit	PDE 1◀	PDE 2	PDE 3	PDE 4	PDE 1◀	PDE 2	PDE 3	PDE 4
$c_1\nabla\cdot\mathbf{v}$	–	–	–	-0.052	-0.052	–	-0.051	-0.051	-0.055
$c_2\Delta\rho$	mm^2 s^{-1}	–	0.016	0.040	0.023	–	0.055	0.040	0.041
$c_3\nabla\cdot(\rho\mathbf{v})$	–	-0.950	-0.950	-1.068	-1.067	-0.945	-1.057	-1.054	-0.985
$c_4\Delta\rho^2$	mm^2 s^{-1}	–	0.047	0.080	0.081	–	-0.076	-0.051	-0.062
$c_5\Delta\lvert\mathbf{v}\rvert^2$	s	–	–	–	0.001	–	–	0.001	0.001
$c_6\nabla\cdot(\rho^2\mathbf{v})$	–	–	–	–	–	–	–	–	-0.313
$c_7\Delta\rho^3$	mm^2 s^{-1}	–	–	–	–	–	0.427	0.341	0.366
$c_8\nabla\cdot(\lvert\mathbf{v}\rvert^2\mathbf{v})$	mm^{-2} s^2	–	–	0.035	0.035	–	0.034	0.034	0.034
$c_9\nabla\cdot(\rho\nabla\lvert\mathbf{v}\rvert^2)$	s	–	–	–	-0.013	–	–	-0.008	-0.007
$c_{10}\nabla\cdot(\lvert\mathbf{v}\rvert^2\nabla\rho)$	s	–	-0.018	-0.039	-0.028	–	-0.036	-0.028	-0.027

TABLE VI. Parameters d_l of the PDE for the velocity dynamics (Fig. 4c) learned from experimental data for self-propelled Quincke rollers (Supplementary Video 2 of Ref. [4]). The dimensions of the coefficients are such that $[\mathbf{v}]$ =mm/s and $[\rho] = 1$, where the density ρ represents the area fraction of rollers of diameter $D_c = 4.8\,\mu$m. The four sparsest PDEs are shown corresponding to the cut-off $n_0 \in \{50, 100\}$ above which the temporal Chebyshev modes in Eq. (3) are set to zero to ignore high frequencies. The sparsest PDEs which reproduce the experimental observations (◀) have coefficients that are close to each other for different values of n_0, and they agree well with corresponding values reported in Ref. [4] (Tab. II).

		$n_0 = 50$				$n_0 = 100$			
Term	Unit	PDE 1	PDE 2◀	PDE 3	PDE 4	PDE 1	PDE 2◀	PDE 3	PDE 4
$d_1\mathbf{v}$	s^{-1}	–	2.281	1.524	1.491	–	1.825	1.252	1.122
$d_2\rho\mathbf{v}$	s^{-1}	–	8.356	5.156	4.745	–	6.135	3.143	3.083
$d_3\lvert\mathbf{v}\rvert^2\mathbf{v}$	mm^{-2} s	–	-2.194	-1.436	-1.382	–	-1.710	-1.095	-0.999
$d_4\nabla\rho$	mm^2 s^{-2}	–	-1.620	-1.711	-2.074	–	-1.689	-2.438	-2.430
$d_5(\mathbf{v}\cdot\nabla)\mathbf{v}$	–	-0.639	-0.674	-0.678	-0.679	-0.662	-0.696	-0.702	-0.702
$d_6\nabla(\nabla\cdot\mathbf{v})$	mm^2 s^{-1}	–	–	–	–	–	–	–	–
$d_7\Delta\mathbf{v}$	mm^2 s^{-1}	–	–	–	–	–	–	–	0.002
$d_8\nabla(\lvert\mathbf{v}\rvert^2)$	–	–	–	–	0.090	–	–	0.169	0.168
$d_9(\nabla\cdot\mathbf{v})\mathbf{v}$	–	–	–	-0.189	-0.190	–	–	-0.178	-0.179
$d_{10}\Delta^2\mathbf{v}$	mm^4 s^{-1}	–	–	–	–	–	–	–	0.000

[1] D. T. Tambe, C. Corey Hardin, T. E. Angelini, K. Rajendran, C. Y. Park, X. Serra-Picamal, E. H. Zhou, M. H. Zaman, J. P. Butler, D. A. Weitz, J. J. Fredberg, and X. Trepat, Nat. Mater. **10**, 469 (2011).

[2] C.-P. Heisenbergand Y. Bellaïche, Cell **153**, 948 (2013).

[3] M. Tennenbaum, Z. Liu, D. Hu, and A. Fernandez-Nieves, Nat. Mater. **15**, 54 (2016).

[4] D. Geyer, A. Morin, and D. Bartolo, Nat. Mater. **17**, 789 (2018).

[5] V. Soni, E. S. Bililign, S. Magkiriadou, S. Sacanna, D. Bartolo, M. J. Shelley, and W. T. M. Irvine, Nat. Phys. **15**, 1188 (2019).

[6] M. Rubenstein, A. Cornejo, and R. Nagpal, Science **345**, 795 (2014).

[7] L. M. Nash, D. Kleckner, A. Read, V. Vitelli, A. M. Turner, and W. T. M. Irvine, Proc. Natl. Acad. Sci. U. S. A. **112**, 14495 (2015).

[8] W. Savoie, T. A. Berrueta, Z. Jackson, A. Pervan, R. Warkentin, S. Li, T. D. Murphey, K. Wiesenfeld, and D. I. Goldman, Sci. Robot. **4**, eaax4316 (2019).

[9] J. Tonerand Y. Tu, Phys. Rev. Lett. **75**, 4326 (1995).

[10] M. C. Marchetti, J. F. Joanny, S. Ramaswamy, T. B. Liverpool, J. Prost, M. Rao, and R. A. Simha, Rev. Mod. Phys. **85**, 1143 (2013).

[11] F. Jülicher, S. W. Grill, and G. Salbreux, Rep. Prog. Phys. **81**, 076601 (2018).

[12] R. Hartmann, P. K. Singh, P. Pearce, R. Mok, B. Song, F. Díaz-Pascual, J. Dunkel, and K. Drescher, Nat. Phys. **15**, 251 (2019).

[13] Y. Li, M. Chen, J. Hu, R. Sheng, Q. Lin, X. He, and M. Guo, Cell Stem Cell (2020).

[14] G. Shah, K. Thierbach, B. Schmid, J. Waschke, A. Reade, M. Hlawitschka, I. Roeder, N. Scherf, and J. Huisken, Nat. Commun. **10**, 5753 (2019).

[15] N. J. Cira, A. Benusiglio, and M. Prakash, Nature **519**, 446 (2015).

[16] W. B. Rogers, W. M. Shih, and V. N. Manoharan, Nat. Rev. Mater. **1**, 16008 (2016).

[17] F. Cichos, K. Gustavsson, B. Mehlig, and G. Volpe, Nat. Mach. Intell. **2**, 94 (2020).

[18] E. H. K. Stelzer, Nat. Meth. **12**, 23 (2015).

[19] R. M. Powerand J. Huisken, Nat. Meth. **14**, 360 (2017).

[20] M. R. Shaebani, A. Wysocki, R. G. Winkler, G. Gompper, and H. Rieger, Nat. Rev. Phys. **2**, 181 (2020).

[21] H. Jeckel, E. Jelli, R. Hartmann, P. K. Singh, R. Mok, J. F. Totz, L. Vidakovic, B. Eckhardt, J. Dunkel, and K. Drescher, Proc. Natl. Acad. Sci. U. S. A. **116**, 1489 (2019).

[22] D. P. Vallette, G. Jacobs, and J. P. Gollub, Phys. Rev. E **55**, 4274 (1997).

[23] M. Bär, R. Hegger, and H. Kantz, Phys. Rev. E **59**, 337 (1999).

[24] J. Bongardand H. Lipson, Proc. Natl. Acad. Sci. U. S. A. **104**, 9943 (2007).

[25] M. Schmidtand H. Lipson, Science **324**, 81 (2009).

[26] S. L. Brunton, J. L. Proctor, and J. N. Kutz, Proc. Natl. Acad. Sci. U.S.A **113**, 3932 (2016).

[27] S. H. Rudy, S. L. Brunton, J. L. Proctor, and J. N. Kutz, Sci. Adv **3**, e1602614 (2017).

[28] S. Maddu, B. L. Cheeseman, C. L. Müller, and I. F. Sbalzarini, Learning physically consistent mathematical models from data using group sparsity (2020), arXiv:2012.06391 [cs.LG].

[29] C. Linghu, S. L. Johnson, P. A. Valdes, O. A. Shemesh, W. M. Park, D. Park, K. D. Piatkevich, A. T. Wassie, Y. Liu, B. An, S. A. Barnes, O. T. Celiker, C.-C. Yao, C.-C. J. Yu, R. Wang, K. P. Adamala, M. F. Bear, A. E. Keating, and E. S. Boyden, Cell **183**, 1682 (2020).

[30] N. Cermak, S. K. Yu, R. Clark, Y.-C. Huang, S. N. Baskoylu, and S. W. Flavell, eLife **9**, e57093 (2020).

[31] P. A. Reinbold, D. R. Gurevich, and R. O. Grigoriev, Phys. Rev. E **101**, 010203(R) (2020).

[32] K. Champion, B. Lusch, J. Nathan Kutz, and S. L. Brunton, Proc. Natl. Acad. Sci. U. S. A. **116**, 22445 (2019).

[33] G.-J. Both, S. Choudhury, P. Sens, and R. Kusters, J. Comp. Phys. **428**, 109985 (2021).

[34] S. Maddu, B. L. Cheeseman, I. F. Sbalzarini, and C. L. Müller, Stability selection enables robust learning of partial differential equations from limited noisy data (2019), arXiv:1907.07810 [math.NA].

[35] J. T. Nardini, R. E. Baker, M. J. Simpson, and K. B. Flores, Learning differential equation models from stochastic agent-based model simulations (2020), arXiv:2011.08255 [math.DS].

[36] L. Felsbergerand P.-S. Koutsourelakis, Communications in Computational Physics **25**, 1259 (2019).

[37] J. Bakarjiand D. M. Tartakovsky, Data-driven discovery of coarse-grained equations (2020), arXiv:2002.00790 [stat.ML].

[38] S. Smith, *Digital signal processing: a practical guide for engineers and scientists* (Elsevier, 2013).

[39] T. A. Driscoll, N. Hale, and L. N. Trefethen, *Chebfun Guide* (Pafnuty Publications, 2014).

[40] K. J. Burns, G. M. Vasil, J. S. Oishi, D. Lecoanet, and B. P. Brown, Phys. Rev. Res. **2**, 023068 (2020).

[41] F. Peruani, A. Deutsch, and M. Bär, Eur. Phys. J. Spec. Top. **157**, 111 (2008).

[42] F. D. C. Farrell, M. C. Marchetti, D. Marenduzzo, and J. Tailleur, Phys. Rev. Lett. **108**, 248101 (2012).

[43] B. Liebchen, M. E. Cates, and D. Marenduzzo, Soft Matter **12**, 7259 (2016).

[44] B. Liebchenand D. Levis, Phys. Rev. Lett. **119**, 058002 (2017).

[45] N. Kruk, J. A. Carrillo, and H. Koeppl, Phys. Rev. E **102**, 22604 (2020).

[46] Y. Sumino, K. H. Nagai, Y. Shitaka, D. Tanaka, K. Yoshikawa, H. Chaté, and K. Oiwa, Nature **483**, 448 (2012).

[47] L. Huber, R. Suzuki, T. Krüger, E. Frey, and A. R. Bausch, Science **361**, 255 (2018).

[48] H. Li, X.-q. Shi, M. Huang, X. Chen, M. Xiao, C. Liu, H. Chaté, and H. P. Zhang, Proc. Natl. Acad. Sci. U.S.A **116**, 777 (2019).

[49] H. Chaté, Annu. Rev. Condens. Matter Phys. **11**, 189 (2020).

[50] F. Giavazzi, C. Malinverno, S. Corallino, F. Ginelli, G. Scita, and R. Cerbino, J. Phys. D: Appl. Phys. **50**, 384003 (2017).

[51] I. H. Riedel, K. Kruse, and J. Howard, Science **309**, 300 (2005).

[52] A. P. Solon, J. Stenhammar, M. E. Cates, Y. Kafri, and J. Tailleur, Phys. Rev. E **97**, 020602 (2018).

[53] E. Wallinand M. Servin, Data-driven model order reduction for granular media (2020), arXiv:2004.03349 [physics.comp-ph].

[54] J. P. Boyd, *Chebyshev and Fourier spectral methods* (Courier Corporation, 2001).

[55] J. C. Masonand D. C. Handscomb, *Chebyshev polynomials* (CRC press, 2002).

[56] O. Brunoand D. Hoch, SIAM J. Numer. Anal **50**, 1581 (2012).

[57] J. L. Aurentzand L. N. Trefethen, ACM Trans. Math. Softw. **43** (2017).

[58] M. Crossand H. Greenside, *Pattern Formation and Dynamics in Nonequilibrium Systems* (Cambridge University Press, Cambridge, 2009).

[59] H. H. Wensink, J. Dunkel, S. Heidenreich, K. Drescher, R. E. Goldstein, H. Löwen, and J. M. Yeomans, Proc. Natl. Acad. Sci. U.S.A **109**, 14308 (2012).

[60] M. James, W. J. Bos, and M. Wilczek, Phys. Rev. Fluids **3**, 061101(R) (2018).

[61] N. Meinshausenand P. Bühlmann, J. R. Statist. Soc. B **72**, 417 (2010).

[62] R. D. Shahand R. J. Samworth, J. R. Statist. Soc. B **75**, 55 (2013).

[63] K. V. Edmond, M. T. Elsesser, G. L. Hunter, D. J. Pine, and E. R. Weeks, Proc. Natl. Acad. Sci. U. S. A. **109**, 17891 (2012).

[64] A. Bricard, J. B. Caussin, N. Desreumaux, O. Dauchot, and D. Bartolo, Nature **503**, 95 (2013).

[65] T. Vicsek, A. Czirok, E. Ben-Jacob, I. Cohen, and O. Shochet, Phys. Rev. Lett. **75**, 1226 (1995).

[66] J. Toner, Y. Tu, and S. Ramaswamy, Ann. Phys. (N. Y). **318**, 170 (2005).

[67] E. Bertin, M. Droz, and G. Grégoire, J. Phys. A **42**, 445001 (2009).

[68] K. P. Champion, S. L. Brunton, and J. N. Kutz, SIAM J. Appl. Dyn. Syst. **18**, 312 (2019).

[69] P. Zheng, T. Askham, S. L. Brunton, J. N. Kutz, and A. Y. Aravkin, IEEE Access **7**, 1404 (2019).

[70] N. M. Mangan, J. N. Kutz, S. L. Brunton, and J. L. Proctor, Proc. R. Soc. London A **473**, 20170009 (2017).

[71] T. Hastie, R. Tibshirani, and J. Friedman, *The Elements of Statistical Learning* (Springer New York Inc., 2001).

[72] A. Reuther, J. Kepner, C. Byun, S. Samsi, W. Arcand, D. Bestor, B. Bergeron, V. Gadepally, M. Houle, M. Hubbell, *et al.*, in *2018 IEEE High Performance extreme Computing Conference (HPEC)* (IEEE, 2018) pp. 1–6.

[73] D. S. Dean, J. Phys. A **29**, L613 (1996).